

Recent advances and innovations in elastocaloric materials for solid-state refrigeration

Yadong Wang(王亚东), Li Wang(王丽), Zhen Chen(陈珍), Haoran Lou(娄浩然), Bin Gong(龚斌), Lian Huang(黄炼), Yandong Wang(王沿东), and Daoyong Cong(从道永)

Citation: Chin. Phys. B, 2026, 35 (**6**): 066201. DOI: 10.1088/1674-1056/ae48b8
http://cpb.iphy.ac.cn; http://iopscience.iop.org/cpb

What follows is a list of articles you may be interested in

Giant mechanocaloric materials for solid-state cooling

Junran Zhang(张俊然), Yixuan Xu(徐逸轩), Shihai An(安世海), Ying Sun(孙莹), Xiaodong Li(李晓东), Yanchun Li(李延春)

Chin. Phys. B, 2020, 29 (**7**): 076202. DOI: 10.1088/1674-1056/ab8a40

Effect of chemical ordering annealing on superelasticity of Ni-Mn-Ga-Fe ferromagnetic shape memory alloy microwires

Yanfen Liu(刘艳芬), Xuexi Zhang(张学习), Hongxian Shen(沈红先), Jianfei Sun(孙剑飞), Qinan Li(李奇楠), Xiaohua Liu(刘晓华), Jianjun Li(李建军), Weidong Cheng(程伟东)

Chin. Phys. B, 2020, 29 (**5**): 056202. DOI: 10.1088/1674-1056/ab8213

First-principles calculations on elastic, magnetoelastic, and phonon properties of Ni_2FeGa magnetic shape memory alloys

Wangqiang He(贺王强), Houbing Huang(黄厚兵), Zhuhong Liu(柳祝红), Xingqiao Ma(马星桥)

Chin. Phys. B, 2018, 27 (**1**): 016201. DOI: 10.1088/1674-1056/27/1/016201

Electronic structures and magnetisms of the $Co_2TiSb_{1-x}Sn_x$ (x=0, 0.25, 0.5) Heusler alloys: A theoretical study of the shape-memory behavior

Wang Li-Ying (王立英), Dai Xue-Fang (代学芳), Wang Xiao-Tian (王啸天), Lin Ting-Ting (林婷婷), Chen Lei (陈磊), Liu Ran (刘然), Cui Yu-Ting (崔玉亭), Liu Guo-Dong (刘国栋)

Chin. Phys. B, 2015, 24 (**12**): 126201. DOI: 10.1088/1674-1056/24/12/126201

TOPICAL REVIEW — Multiferroicity and multicaloric effects

Recent advances and innovations in elastocaloric materials for solid-state refrigeration

Yadong Wang(王亚东)[1], Li Wang(王丽)[1], Zhen Chen(陈珍)[2], Haoran Lou(娄浩然)[1], Bin Gong(龚斌)[1], Lian Huang(黄炼)[3], Yandong Wang(王沿东)[1], and Daoyong Cong(从道永)[1,†]

[1] *State Key Laboratory for Advanced Metals and Materials, University of Science and Technology Beijing, Beijing* 100083, *China*
[2] *School of Materials Science and Engineering, Xi'an University of Technology, Xi'an* 710048, *China*
[3] *Department of Mechanical Engineering, Hunan Institute of Engineering, Xiangtan* 411101, *China*

(Received 13 November 2025; revised manuscript received 8 February 2026; accepted manuscript online 23 February 2026)

Elastocaloric refrigeration technology is a highly efficient and environmentally friendly solid-state alternative to conventional vapor-compression refrigeration systems, leveraging the elastocaloric effects generated during the stress-induced martensitic transformations in shape memory alloys (SMAs). The cooling performance of this emerging technology primarily depends on the comprehensive properties of SMAs, which serve as the refrigerants. To date, various SMAs, such as Ni–Mn-based, Ni–Ti-based, Co-based, Ni–Fe–Ga-based, and Cu-based alloys, have demonstrated significant elastocaloric effects. However, the development of elastocaloric refrigeration applications is often severely hindered by other crucial properties of these SMAs, such as transformation temperature, transformation stress, stress hysteresis, coefficient of performance (COP), fatigue resistance, and cost. In this article, we provide a concise overview of recent research progress in elastocaloric performance across various SMAs, with a focus on the optimization strategies and the underlying microstructural mechanisms. Meanwhile, this review aims to provide actionable guidance and a comprehensive roadmap for the development of high-performance SMAs, facilitating the transition from laboratory-scale breakthroughs to practical elastocaloric refrigeration applications in the near future.

Keywords: solid-state refrigeration, elastocaloric effect, shape memory alloys, martensitic transformation

PACS: 62.20.fg, 61.66.Dk, 61.82.Bg

DOI: 10.1088/1674-1056/ae48b8 **CSTR:** 32038.14.CPB.ae48b8

1. Introduction

Refrigeration technology has become essential in various aspects of modern society, including cold storage, cold-chain transportation, temperature control for residential and industrial space, as well as agricultural production. The traditional vapor-compression refrigeration technology remains the most widely used and commercially viable refrigeration method, having been in large-scale use for over a hundred years.[1] Nowadays, vapor-compression refrigeration systems primarily employ gaseous hydrofluorocarbons (HFCs) as refrigerants, which achieve the refrigeration effect through liquid-to-gas phase transformation accompanied by the release and absorption of latent heat. However, HFCs are potent greenhouse gases with global warming potentials (GWP) significantly higher than that of CO_2. Their leakage contributes significantly to global warming and exacerbates environmental problems.[2] Hence, it is imperative to explore innovative refrigeration technologies with less environmental impact. The emerging green solid-state refrigeration technologies, which utilize thermal effects from solid-solid transformations, have attracted substantial research attention in recent decades due to their environmental advantages and absence of direct greenhouse gas emissions.[3–5] These technologies can be classified into four primary categories based on their external driving stimuli: magnetocaloric (magnetic field-induced), electrocaloric (electric field-induced), barocaloric (pressure-induced), and elastocaloric (uniaxial stress-induced) refrigeration systems.[6–18] Among these, elastocaloric refrigeration technology was identified by the U.S. Department of Energy in 2014 as one of the most promising solid-state alternatives to conventional refrigeration technologies and has since received considerable attention.[19] High-performance elastocaloric materials, serving as the core of elastocaloric refrigeration devices, play a crucial role in advancing the practical application of this refrigeration technology. Currently, shape memory alloys (SMAs, including Ni–Ti-based, Cu-based, Co-based, Ni–Fe–Ga-based, and Ni–Mn-based alloys) have demonstrated significant elastocaloric effects, which arise from stress-induced first-order martensitic transformation, thereby making them the predominant choice for elastocaloric materials.[7,20–27] Among various SMAs, Ni–Mn-based Heusler-type SMAs and Ni–Ti-based SMAs stand out due to either a colossal elastocaloric effect or long-term functional stability, which serve as two critical performance met-

[†]Corresponding author. E-mail: dycong@ustb.edu.cn

© 2026 Chinese Physical Society and IOP Publishing Ltd. All rights, including for text and data mining, AI training, and similar technologies, are reserved.

rics for practical elastocaloric refrigeration applications.

Essentially, the elastocaloric effect refers to a thermal response that fundamentally relies on the release and absorption of latent heat as well as changes in entropy during the reversible martensitic transformation induced by cyclic uniaxial loading and unloading.[28] The testing temperature must be above the reverse martensitic transformation finish temperature (A_f), which is a prerequisite for achieving effective elastocaloric effects through complete transformation during unloading. Notably, since primary refrigeration applications operate around room temperature, the A_f of elastocaloric materials should be below room temperature to facilitate efficient room-temperature refrigeration.[29] Moreover, the critical stress for martensitic transformation increases linearly as the ambient temperature increases.[30] Therefore, the testing temperature cannot significantly exceed A_f; otherwise, the driving force required for refrigeration would increase. The magnitude of elastocaloric effects can be well quantified by the adiabatic temperature change ΔT_{ad} and the isothermal entropy change ΔS_{iso}.[31] The ΔT_{ad} can be directly measured using a thermocouple attached to the specimen surface or a non-contact infrared camera. Meanwhile, ΔS_{iso} can be indirectly calculated from stress–strain curves obtained at different testing temperatures, based on the Maxwell relation[8]

$$\Delta S_{iso} = \frac{1}{\rho}\int_0^{\varepsilon}\left(\frac{\partial \sigma}{\partial T}\right)_{\varepsilon} \mathrm{d}\varepsilon, \tag{1}$$

where ρ denotes the density of the elastocaloric material. Furthermore, the ΔT_{ad} can be approximately estimated by the following relation:[31]

$$\Delta T_{ad} \approx \frac{T}{C_p}\Delta S_{iso}, \tag{2}$$

where C_p is the specific heat capacity of the material. A large ΔS_{iso} often leads to a large ΔT_{ad} and significant elastocaloric effects. Essentially, the larger lattice distortion during martensitic transition reflects a more pronounced first-order phase transformation and is closely associated with a larger ΔS_{iso} value.[22]

Additionally, the cyclic stability of the elastocaloric effect is a critical determinant for practical applications. Specifically, fatigue of most elastocaloric materials represents a major bottleneck for the realistic implementation of elastocaloric refrigeration, encompassing both functional fatigue (the degradation of the elastocaloric effect and its reversibility) and structural fatigue (the loss of material integrity). To achieve superior elastocaloric performance, excellent mechanical properties, particularly high strength combined with non-brittleness, are essential prerequisites. These mechanical characteristics play a critical role in inhibiting dislocation motion and preventing defect generation and accumulation during cyclic loading, thereby ensuring complete induction, as well as excellent reversibility and long-term cyclic stability of the martensitic transformation.[32] The coefficient of performance (COP) is an important property used to quantify the refrigeration efficiency of elastocaloric materials. COP is defined as the amount of cooling produced per unit of dissipated work and is calculated as the ratio of the cooling power (ΔQ)) to the input work (ΔW)):[33]

$$\mathrm{COP} = \frac{\Delta Q}{\Delta W}. \tag{3}$$

Here, ΔQ is the extracted latent heat, which can be estimated by[34,35]

$$\Delta Q = C_p \cdot \Delta T_{ad}, \tag{4}$$

ΔW, corresponding to the area of the stress hysteresis loop, can be integrated from the stress–strain curve.[36] Therefore, a highly efficient elastocaloric refrigeration system requires materials that exhibit low ΔW and high ΔQ during stress-induced martensitic transformation. Notably, COP can be classified into two types: $\mathrm{COP}_{\mathrm{ReverseBrayton}}$ and $\mathrm{COP}_{\mathrm{ReverseStirling}}$, which correspond to the reverse Brayton cycle and the reverse Stirling cycle, respectively.[37] Specifically, the reverse Brayton cycle consists of two isostress heat transfer processes and two isentropic phase transfer processes. The reverse Stirling cycle consists of two isostress heat transfer processes and two isothermal phase transfer processes. As a result, the measured COP value of an elastocaloric material depends on the specific cycle configuration during the measurements.

As is known, hysteresis is an inherent and unavoidable characteristic of first-order phase transformations, stemming from energy dissipation through frictional work and the generation of crystal defects (such as dislocations) during the reversible transformation, which could lead to material fatigue and failure.[32,38–41] Consequently, apart from a large ΔT_{ad}, a smaller stress hysteresis, corresponding to less energy dissipation, is also desirable for optimizing the elastocaloric performance. Additionally, another important elastocaloric performance metric is the specific adiabatic temperature change $\Delta T_{ad}/\sigma$,[42] denoting the adiabatic temperature variation per unit of applied stress and partially reflecting the refrigeration efficiency of an elastocaloric material. A large $\Delta T_{ad}/\sigma$ demonstrates a clear advantage for the application in elastocaloric refrigeration.

Up to now, numerous research efforts have been devoted to the exploration and development of high-performance elastocaloric materials. Notably, maximizing one material property for elastocaloric applications often comes at the expense of other critical properties required for practical implementation. Here, we present a comprehensive review of recent advances in enhancing elastocaloric performance and investigating the underlying microstructural mechanisms in various

SMAs. This review aims to provide guidance and future perspectives for developing high-performance elastocaloric materials and elastocaloric refrigeration prototypes.

2. Ni–Mn-based elastocaloric alloys

Ni–Mn-based Heusler-type magnetic SMAs are among the earliest and most extensively researched materials considered as promising candidates for elastocaloric refrigeration, primarily taking into account the large unit cell volume change $\Delta V/V$ in the master alloy $Ni_{50}Mn_{50}$ alloy,[43] which may lead to large elastocaloric effects. Usually, Ni–Mn-based SMAs exhibit intrinsic brittleness, originating from poor grain boundary cohesion,[44] which hinders their practical implementation in elastocaloric refrigeration. This mechanical limitation can lead to premature structural failure during stress-induced martensitic transformation, compromising the elastocaloric response and the long-term operational stability necessary for commercial elastocaloric applications.

Cong *et al.*[22] proposed a novel design strategy based on boron (B) microalloying in all-d-metal Ni–Mn–Ti alloys, which exhibit not only a large $\Delta V/V$ during the phase transformation but also improved mechanical properties. First, all-d-metal Ni–Mn–Ti alloys are selected due to their relatively low intrinsic brittleness compared to other Ni–Mn-based alloys.[45] Second, B microalloying, which has been proven effective in enhancing the ductility and processability of structural intermetallics such as Ni_3Al, Ni_3Fe, and FeAl,[46–49] further strengthens grain boundary cohesion in Ni–Mn–Ti alloys, despite a slight reduction in ΔS_{iso} upon B doping. Meanwhile, the tunable transformation temperature can be brought down to slightly below room temperature by adjusting the Ti and B content, enabling the achievement of a room-temperature elastocaloric effect. Notably, significantly large $\Delta V/V$ values above 1.89% are obtained during martensitic transformation in the $(Ni_{50}Mn_{50-x}Ti_x)_{99.8}B_{0.2}$ ($x = 18$ and 18.5) alloys, which are much higher than those reported in other Ni–Mn-based Heusler SMAs (Fig. 1(a)).[22] Consequently, as shown in Fig. 1(b), the bulk polycrystalline $(Ni_{50}Mn_{31.5}Ti_{18.5})_{99.8}B_{0.2}$ alloy exhibits a strikingly high ΔT_{ad} value of 31.5 K during unloading at near room temperature ($\sim$ 308 K). This colossal elastocaloric effect far exceeds that directly measured in all elastocaloric, electrocaloric, and barocaloric materials at that time. This remarkable result, achieved in bulk polycrystalline materials that are inexpensive to fabricate and can be easily scaled up, represents a significant step forward toward the large-scale application of high-efficiency and environment-friendly elastocaloric refrigeration technologies.

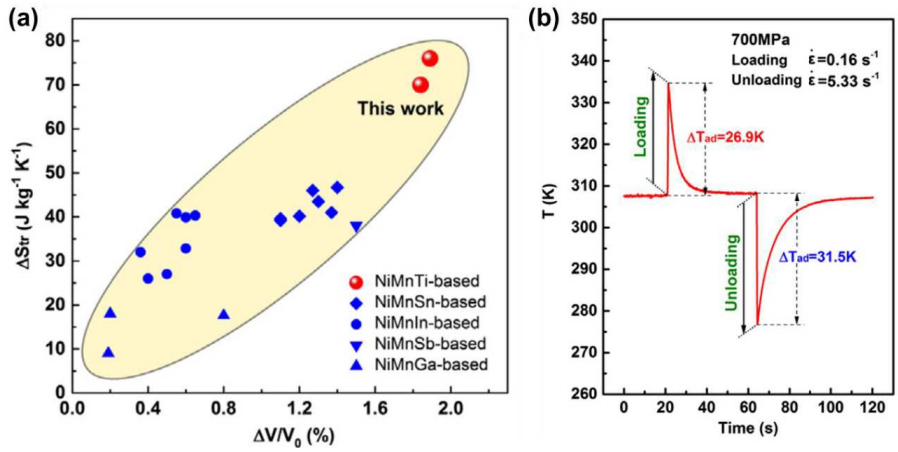


Fig. 1. (a) Correlation between the transformation entropy change ΔS_{tr} and the unit cell volume change $\Delta V/V$ across the transformation in Ni–Mn-based Heusler alloys. (b) Temperature variation in the $(Ni_{50}Mn_{31.5}Ti_{18.5})_{99.8}B_{0.2}$ alloy as a function of time during loading, holding, and unloading stages. The maximum applied stress is 700 MPa, and the strain rate $\dot{\varepsilon}$ for loading and unloading is displayed in the figure. Adapted from Ref. [22].

During the loading stage of elastocaloric cooling cycles, stress-induced martensitic variants often form asynchronously and with misaligned orientations across adjacent grains, which generates localized stress concentrations and crack initiation at grain boundaries.[50,51] In Ni–Mn-based intermetallic SMAs, the problem is further exacerbated by intrinsic grain boundary brittleness.[46] Consequently, these combined factors ultimately lead to degradation of the cyclic stability in elastocaloric performance. Yang *et al.*[52] significantly improved the cyclic stability of Ni–Mn–In intermetallic alloys through B microalloying. In addition to enhancing grain boundary cohesion, which suppresses fatigue crack initiation and propagation along grain boundaries during stress-induced martensitic transformation, B addition also leads to grain refinement, thereby increasing both yield strength and fracture strength in B-doped alloys. This strengthening mechanism is comparable to that observed in TiAl structural intermetallics.[53] Therefore, the excellent mechanical properties effectively inhibit localized plastic deformation by dislocation slip during phase transformation, which can give rise to crack ini-

tiation during cyclic loading. Moreover, the misorientation between neighboring grains is reduced in fine-grained alloys, promoting more synchronized stress-induced transformations across adjacent grains and thereby alleviating stress concentrations at grain boundaries. As a result, the optimized novel $(Ni_{51.5}Mn_{33}In_{15.5})_{99.7}B_{0.3}$ alloy exhibits a fine-grained microstructure with a grain size of approximately 20 μm, achieves a moderate room-temperature ΔT_{ad} of up to 6.6 K during unloading at 303 K, and maintains a stable elastocaloric effect with negligible degradation over 150 cycles (Figs. 2(a)–2(c)).[52] These advantages make the designed Ni–Mn–In–B alloy a promising candidate for potential room-temperature elastocaloric refrigeration applications. In contrast, the ternary B-free $Ni_{51.5}Mn_{33}In_{15.5}$ alloy, which has a coarse-grained microstructure with a grain size of approximately 120 μm, exhibits rapid degradation of the elastocaloric effect after only about 20 cycles and ultimately fractures by the 23rd cycle (Figs. 2(d) and 2(e)).

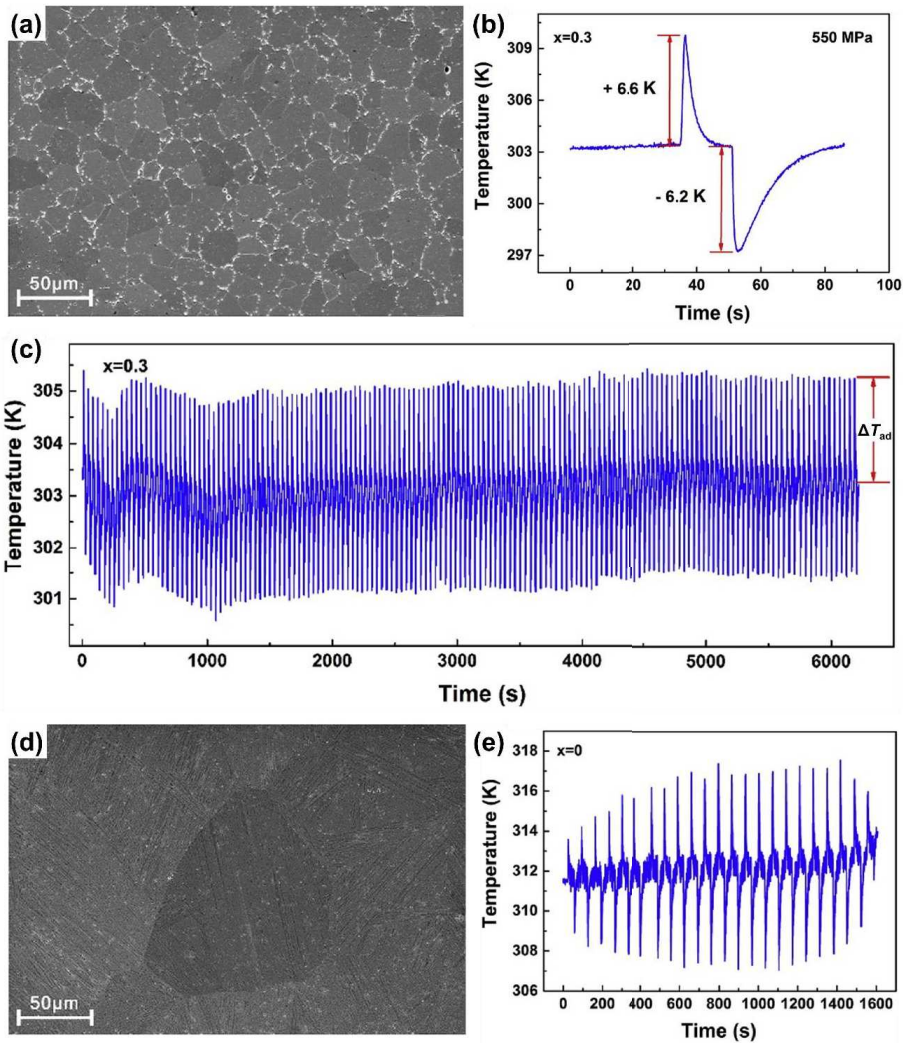


Fig. 2. (a) SEM secondary electron micrographs of the $(Ni_{51.5}Mn_{33}In_{15.5})_{99.7}B_{0.3}$ alloy at room temperature. (b) Temperature variation of the $(Ni_{51.5}Mn_{33}In_{15.5})_{99.7}B_{0.3}$ alloy during loading up to 550 MPa, holding, and unloading with a high strain rate of 4.2×10^{-2} s^{-1}, shown as a function of time. (c) Temperature variation of the the $(Ni_{51.5}Mn_{33}In_{15.5})_{99.7}B_{0.3}$ alloy during loading up to 300 MPa, holding, and unloading at a high strain rate of 1.4×10^{-2} s^{-1}, shown as a function of time. (d) SEM secondary electron micrographs of the $Ni_{51.5}Mn_{33}In_{15.5}$ alloy at room temperature. (e) Temperature variation of the $Ni_{51.5}Mn_{33}In_{15.5}$ alloy during loading up to 300 MPa, holding, and unloading at a high strain rate of 1.4×10^{-2} s^{-1}, shown as a function of time. Adapted from Ref. [52].

Subsequently, Yang *et al.*[23] further employed the simultaneous substitution of Fe for In and Ni to counteract the effect of B microalloying on the transformation temperature. Moreover, the formation of B-rich nanoscale $NiBH^{+}$ clusters along grain boundaries, as shown in Fig. 3(a), effectively traps hydrogen, thereby suppressing hydrogen embrittlement and enhancing grain boundary strength. Through the synergistic effects of B microalloying and Fe substitution, the $(Ni_{51}Mn_{33}In_{14}Fe_2)_{99.4}B_{0.6}$ alloy achieves an A_f slightly below room temperature, indicating a promising operational temperature range for elastocaloric refrigeration applications near room temperature. The elastocaloric effect of the $Ni_{51}Mn_{33}In_{14}Fe_2$ alloy remained nearly unchanged over 109 loading–unloading cycles before fracture occurred, demonstrating that Fe substitution partially improves the cyclic stability of the elastocaloric effect compared

to the ternary $Ni_{51.5}Mn_{33}In_{15.5}$ alloy.[23] Notably, the B-doped $(Ni_{51}Mn_{33}In_{14}Fe_2)_{99.4}B_{0.6}$ alloy, with an average grain size of approximately 15 μm, exhibits significantly improved cyclic stability, maintaining a consistent ΔT_{ad} of 5.6 K with no observable degradation over 2700 cycles (Fig. 3(b)), and showing no structural damage after testing. This highlights that the $(Ni_{51}Mn_{33}In_{14}Fe_2)_{99.4}B_{0.6}$ alloy achieves a remarkable enhancement in cyclic stability, which is two orders of magnitude greater than that of conventional Ni–Mn-based SMAs. Tang *et al.*[54] simultaneously introduced Cu and B into the Ni–Mn–In alloy, achieving both a high ΔT_{ad} and improved cyclic stability. The $(Ni_{52}Mn_{31}In_{16}Cu_1)_{99.8}B_{0.2}$ alloy exhibits a large ΔT_{ad} of 9.5 K during unloading after the application of a stress of 220 MPa at room temperature, yielding a high $\Delta T_{ad}/\sigma$ value of approximately 43.2 K·GPa^{-1}. Even after 100 loading–unloading cycles at a strain of 3%, the ΔT_{ad} remains stable in both the loading and unloading processes, with no noticeable degradation. The average ΔT_{ad} values are approximately 7.5 K during loading and 6.8 K during unloading. The remarkable functional performance can be attributed to the excellent mechanical properties induced by Cu and B co-doping, which enable a large transformation fraction in the Ni–Mn–In–Cu–B alloy. In contrast, the ternary Ni–Mn–In alloy exhibits poor mechanical properties due to the intrinsic brittleness of its intermetallic matrix, resulting in a low ΔT_{ad} of only 1 K.[54]

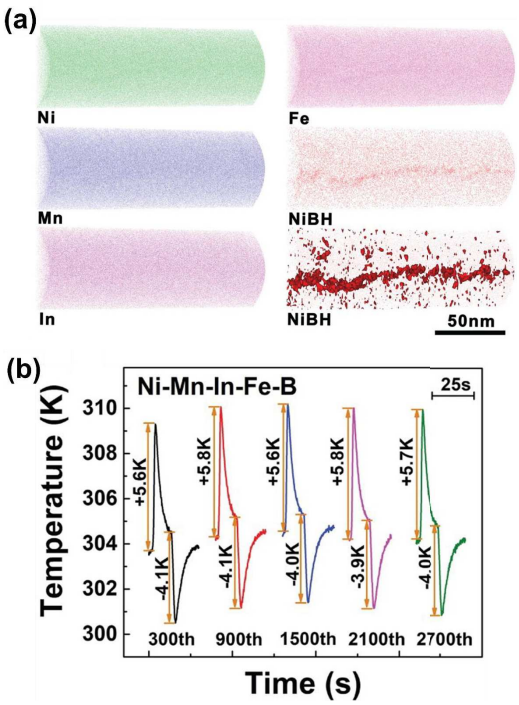


Fig. 3. (a) The 3D atom probe tomography (APT) reconstructions of the $(Ni_{51}Mn_{33}In_{14}Fe_2)_{99.4}B_{0.6}$ tip specimen, showing the atomic distributions of Ni, Mn, In and Fe, as well as the $NiBH^+$ segregation around the grain boundary, together with the iso-concentration surface of NiBH+ at 0.8% (lower right panel). (b) Temperature variation as a function of time recorded during the 300th, 900th, 1500th, 2100th and 2700th loading, holding, and unloading cycles for the $(Ni_{51}Mn_{33}In_{14}Fe_2)_{99.4}B_{0.6}$ alloy. Adapted from Ref. [23].

Owing to the highly anisotropic characteristics of the martensite formed during the phase transition process, the transformation strain is highly dependent on crystallographic orientation.[55] As demonstrated by Hernández-Navarro *et al.* in the nominal $Ni_{50}Mn_{32}In_{16}Cr_2$ polycrystalline alloy, the applied stress required to induce martensitic transformation varies notably with crystallographic orientation.[56] Specifically, the [001] direction of the austenite phase exhibits the highest resolved shear stress factor (RSSF), followed by the [111] direction and finally the [110] direction, analogous to Schmid's law. A higher RSSF indicates that a lower stress is required to trigger the martensitic transformation compared to orientations with a lower RSSF. As a result, the [001] orientation has a lower critical stress for inducing martensite and thus facilitates a more complete martensitic transformation. The crystallographic orientation also strongly influences the mechanical yielding behavior of SMAs. Additionally, functional and structural fatigue in elastocaloric materials is closely associated with the interplay between stress-induced martensitic transformation and irreversible plastic deformation, which includes dislocation slip and/or martensite stabilization. Given that both phase transformation and dislocation slip are orientation-sensitive, the predominant deformation mechanism under cyclic loading can be effectively regulated by controlling the preferred crystallographic orientation in single crystals or textured polycrystals.[57,58] The corresponding micromechanisms (dislocation accumulation, retained martensite, or a combination of both) underlying functional fatigue therefore vary with crystallographic orientations, ultimately affecting fatigue life.

Textured columnar polycrystalline SMAs can effectively reduce stress concentrations at grain boundaries and promote deformation compatibility between adjacent grains during phase transformation, which suppresses dislocation activities and minimizes crack initiation during cyclic transformation. Highly textured columnar polycrystals are often fabricated by directional solidification. Notably, the formation of a preferred orientation results from a competitive growth process among grains with different orientations. Therefore, during the directional solidification process, solidification parameters of the temperature gradient (G) and the solidification rate (R) synergistically influence the microstructure morphology and the crystal orientation, as demonstrated by Li *et al.*[59] in the $Co_{32}Ni_{40}Al_{28}$ alloys. Specifically, a higher G/R ratio suppresses constitutional undercooling at the solid–liquid interface, which not only maintains a low nucleation rate at the interface but also promotes crystal growth in a planar mode, ultimately leading to coarse columnar grains with a preferred orientation. In contrast, a lower G/R ratio contributes to increased undercooling at the solid–liquid interface, resulting in a higher nucleation rate. The growth kinetics under this condi-

tion enable multiple crystal planes to develop, facilitating cellular or dendritic growth of the crystals, and thus the number of orientations increases.

As demonstrated in recent literature,[60] a colossal ΔT_{ad} of up to 37.3 K was obtained during unloading at 313 K in a $\langle 001\rangle_A$ oriented $Ni_{49}Mn_{33}Ti_{18}$ alloy prepared by directional solidification. Additionally, Guan *et al.*[24] chose Ni–Co–Mn–Ti all-d-metal Heusler-type alloys, which possess the favorable mechanical properties as outlined before, and integrated them with the directional solidification technique using the Bridgman method to minimize grain boundary density and suppress crack initiation, thereby giving rise to high mechanical performance. The polycrystalline all-d-metal alloy with a composition of $Ni_{36.6}Co_{12.8}Mn_{34.7}Ti_{15.9}$ exhibits a suitable A_f of 280 K, slightly below room temperature, and a strong $\langle 001\rangle_A$ preferred orientation aligned with the solidification direction. Owing to these characteristics, this alloy achieves high compressive strength and a large fracture strain of 17.7%.[24] The critical stress of the martensitic transformation is as low as 92 MPa at 293 K, as illustrated in Fig. 4(a), indicating a small external stress field and reduced input work required for elastocaloric refrigeration. A moderate ΔT_{ad} of 19.8 K was obtained during loading at 8% strain under a relatively low driving stress of approximately 338 MPa at a high strain rate (Fig. 4(b)). The corresponding $\Delta T_{ad}/\sigma$ is 58.6 K·GPa^{-1}, highlighting an obvious advantage for its application in elastocaloric refrigeration. Furthermore, as displayed in Fig. 4(c), a ΔT_{ad} of about 6 K remains stable over more than 10000 cycles, suggesting excellent reversibility of the elastocaloric effect. This extraordinary mechanical and functional performance is primarily attributed to the d–d chemical bonding, a large $\Delta V/V$, and the highly preferred crystallographic orientation induced by directional solidification in Ni–(Co)–Mn–Ti Heusler-type SMAs.

Moreover, Guan *et al.*[58] improved the elastocaloric effect and enhanced the cyclic stability of Ni–Mn-based Heusler-type alloys by combining texture control with B-induced grain boundary strengthening. The $(Ni_{50}Mn_{28}Fe_{2.5}Ti_{19.5})_{99.4}B_{0.6}$ alloy exhibits a single austenite phase at room temperature and consists of coarse columnar grains with a strong $\langle 001\rangle_A$ crystallographic orientation aligned along the directional solidification direction (SD). There are two types of secondary phases, including the (Ni, Mn, Fe)$_3$Ti phase and a B-rich secondary phase. The B-rich phase is predominantly distributed along grain boundaries, which is consistent with findings from previous studies.[61] As a result, the alloy achieves a high ultimate compressive strength along with a large fracture strain at 303 K. A large ΔT_{ad} of 24.5 K is achieved during rapid removal of a maximum strain of 8%, corresponding to a relatively low driving stress of approximately 430 MPa. Furthermore, a stable ΔT_{ad} of approximately 5.8 K is maintained over more than 20000 cycles at a strain level of 3.5%, outperforming some conventional Ni–Fe–Ga-based, Co-based, and Cu-based alloys.

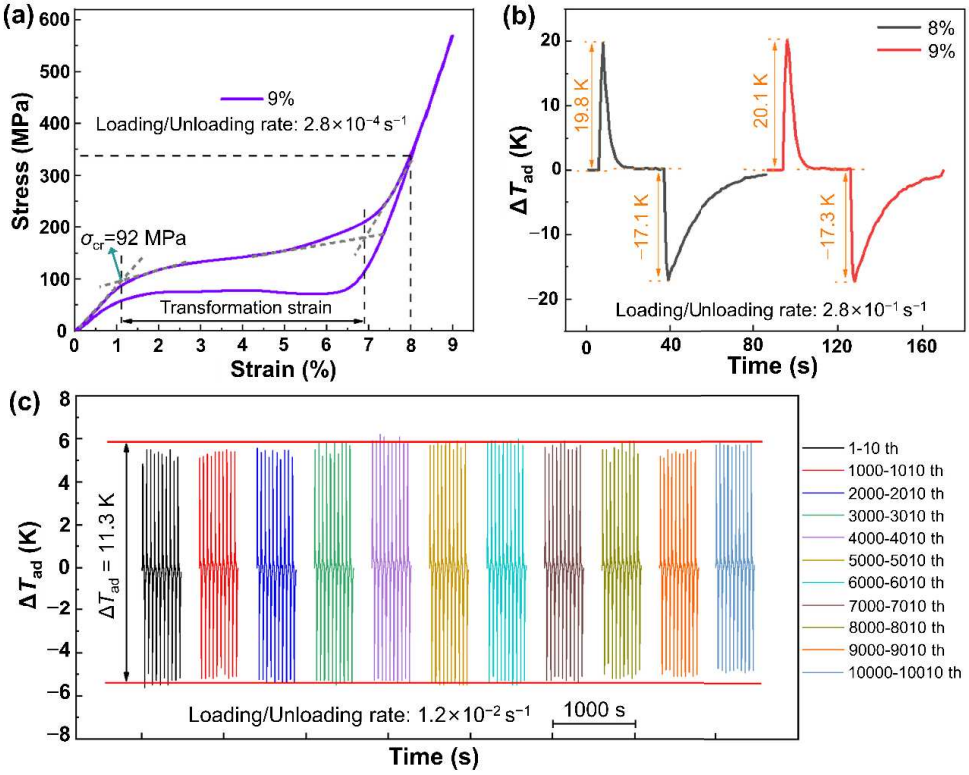


Fig. 4. (a) Compressive superelastic response of $Ni_{36.6}Co_{12.8}Mn_{34.7}Ti_{15.9}$ directionally solidified alloy at 293 K. (b) Time dependence of ΔT_{ad} under various compressive strains at a strain rate of 2.8×10^{-2} s^{-1}. (c) Selective temperature profiles during cyclic loading/unloading tests at a strain rate of 1.2×10^{-2} s^{-1}. Adapted from Ref. [24].

Recently, Zhang *et al.*[62] reported a novel directionally solidified Heusler-type Ni–Mn–Ti SMA with a nominal composition of $Ni_{46}Mn_{32.5}Ti_{17.5}Si_4$, which exhibits exceptional cyclic stability over one million cycles at room temperature and maintains a significant ΔT_{ad} of 12.7 K during unloading after prolonged cycling under a moderate stress of 566 MPa. These outstanding elastocaloric properties arise from the synergistic interaction between non-transforming Mn_2Ti precipitate hardening, induced by Si substitution for Ni, and highly textured columnar austenite grains with a preferred $\langle 001\rangle_A$ orientation. As can be seen in Fig. 5, the hard Mn_2Ti precipitates, present in a large volume fraction ($\sim$ 30%), effectively alter the fracture mode from intergranular to transgranular, thereby significantly enhancing the overall mechanical strength. Highly textured columnar grains with a preferred $\langle 001\rangle_A$ orientation, achieved via directional solidification, enhance strain compatibility at grain boundaries and mitigate internal constraints arising from misoriented grains during phase transformation.[62] This leads to enhanced yield strength and a lower critical driving stress for phase transformation. As a consequence, the relatively low critical driving stress (σ_{cr} = 254 MPa) in the textured dual-phase $Ni_{46}Mn_{32.5}Ti_{17.5}Si_4$ alloy, which is significantly lower than its yield strength, effectively suppresses the tendency of dislocation-mediated plasticity during repeated stress-induced phase transformations. This enables remarkable functional stability and simultaneously enhances the cooling capacity of the Ni–Mn–Ti–Si alloys.

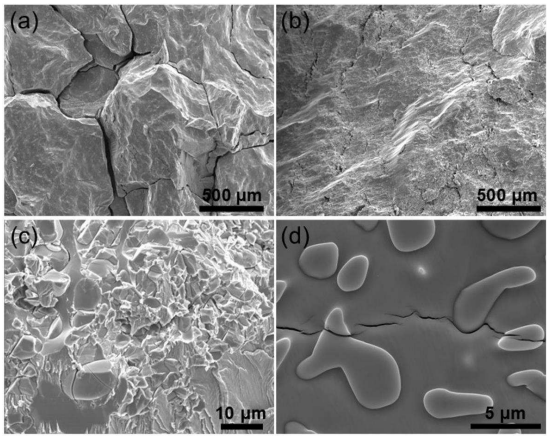


Fig. 5. (a) Fractured surface morphology of the arc-melted $Ni_{49}Mn_{32.5}Ti_{17.5}Si_1$ alloy. (b) Fractured surface morphology of the arc-melted $Ni_{46}Mn_{32.5}Ti_{17.5}Si_4$ alloy. (c) Fractured surface morphology at higher magnification of the arc-melted $Ni_{46}Mn_{32.5}Ti_{17.5}Si_4$ alloy. (d) Local micrograph of crack propagation for the arc-melted $Ni_{46}Mn_{32.5}Ti_{17.5}Si_4$ alloy. Reproduced with permission from Ref. [62].

In addition to macroscopic applications, microelectronics, microsensors, and lab-on-a-chip systems demand localized refrigeration and precise temperature control at the microscale. Low-dimensional elastocaloric materials, such as films, ribbons, and wires with high surface-to-volume ratios, offer advantages over bulk alloys due to their enhanced heat transfer, enabling higher cycling frequencies. Chen *et al.*[63] developed an oligocrystalline $Ni_{50}Mn_{34}Fe_5In_{11}$ microwire with a $\langle 001\rangle_A$ orientation nearly aligned along the axial direction, fabricated via the Taylor–Ulitovsky method. By combining alloying strategies involving dopants (In, Fe) in the binary $Ni_{50}Mn_{50}$ with tailored fabrication techniques, the resulting preferentially oriented $Ni_{50}Mn_{34}Fe_5In_{11}$ microwire exhibits a suitable A_f of 283.3 K, slightly lower than room temperature, and a large $\Delta V/V$ of 1.24% across the martensitic transformation. Moreover, the alignment of the $\langle 001\rangle_A$ crystallographic direction with the loading direction eliminates constraints imposed by grains of differing orientations during stress-induced martensitic transformation, thereby reducing the driving force required for the phase transition. As a result, a ΔT_{ad} of 5.7 K was directly measured upon removal of a relatively low maximum applied stress of 120 MPa at 299 K. An exceptionally high $\Delta T_{ad}/\sigma$ up to 47.5 K·GPa^{-1} is obtained, which is the highest value among all reported low-dimensional elastocaloric materials.[63] The large room-temperature ΔT_{ad}, ultra-high $\Delta T_{ad}/\sigma$, and significant surface-to-volume ratio highlight the promising potential of this Ni–Mn–Fe–In microwire for use in miniaturized and compact refrigeration devices.

As mentioned above, numerous studies have been conducted on elastocaloric cooling based on Ni–Mn-based SMAs. To clearly illustrate the merits of various Ni–Mn-based elastocaloric materials for cooling applications, we compared multiple properties of several representative SMAs from the aforementioned studies on a radar chart (Fig. 6). As shown in Fig. 6, existing alloys generally exhibit significant advantages in one or more specific properties, rather than achieving balanced and simultaneous optimization across all key elastocaloric cooling metrics.

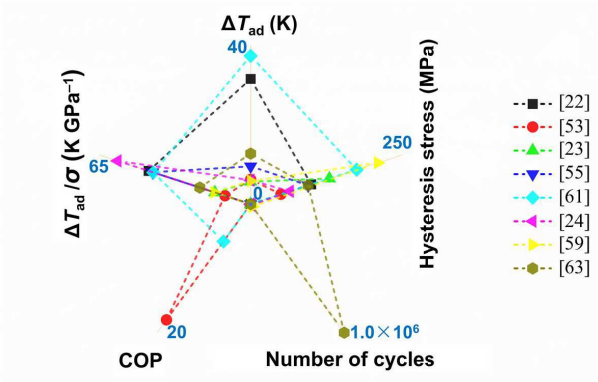


Fig. 6. Comprehensive comparison of multiple properties of various Ni–Mn-based SMAs as elastocaloric materials.

3. Ni–Ti-based elastocaloric alloys

Near-equiatomic Ni–Ti alloys were first developed by the U.S. Naval Ordnance Laboratory in the 1960s. The elastocaloric effect in NiTi alloys, achieving a ΔT_{ad} of approximately 14 K, was first demonstrated by British researchers

Quarin and Prince.[64] Subsequently, Cui *et al.*[34] investigated the elastocaloric effect in a 3 mm-diameter Ni–Ti wire and achieved a large ΔT_{ad} of 17 K. Thereafter, research on the elastocaloric effect in Ni–Ti-based alloys gained increasingly widespread attention. Although near-equiatomic Ni–Ti alloys exhibit substantial latent heat and favorable mechanical properties that distinguish them from other elastocaloric materials, their autocatalytic and avalanche-like phase transformation behavior, combined with lattice mismatch at the B2/B19′ interface, promotes plastic deformation through dislocation activity and leads to the retention of residual martensite.[65] As a result, the gradual accumulation of localized defects (such as dislocations and residual martensite) during cyclic loading leads to the degradation of the elastocaloric response and, ultimately, structural fatigue failure in Ni–Ti-based alloys, which hinders their commercial viability as novel solid-state refrigerants. Specifically, the fatigue life of elastocaloric materials is primarily governed by the following multiple factors: the compatibility of the martensite-austenite interfaces, the critical stress for phase transformation, the yield strength, and the loading modes (compressive/tensile). In recent years, to optimize functional stability and engineering practicability, researchers have concentrated on alleviating microscopic strain incompatibility at phase interfaces via element doping, strengthening the matrix strength by means of grain refinement, precipitation hardening, and nanocomposite engineering, and optimizing the difference between the martensitic transformation stress and the yield stress.

The addition of third or fourth elements represents a common and effective strategy for enhancing yield strength through solid solution strengthening.[66,67] However, in elastocaloric alloys, such dopants often affect the martensitic phase transformation characteristics, thereby influencing functional performance. Up to now, researchers have examined and screened various doping elements (such as Cu, Fe, V, and Ga) to simultaneously improve mechanical and elastocaloric properties. Among these, Cu, which partially substitutes for Ni atoms, effectively reduces hysteresis and energy dissipation during phase transformation, modifies the phase transition behavior, and improves cyclic stability. A Ti-rich Ni–Ti–Cu film prepared via magnetron sputtering technique has demonstrated exceptional durability, sustaining up to 1×10^7 cycles without performance degradation. The significant improvement in cyclic stability is primarily attributed to the enhanced geometric compatibility between different phases and the formation of coherent Ti_2Cu precipitates.[68]

Bulk alloys exhibiting large near-room-temperature ΔT_{ad} and excellent functional stability are considered essential for current large-scale elastocaloric refrigeration applications. Yang *et al.* [29] prepared a bulk polycrystalline solution-treated $(Ni_{42.5}Ti_{50}Cu_{7.5})_{99}Co_1$ (Cu7.5) alloy exhibiting a large elastocaloric effect (ΔT_{ad} = 14.4 K, Fig. 7(a)), low stress hysteresis (only 90 MPa), a high $COP_{ReverseBrayton}$ (up to 16.7), and room-temperature operational capability. As shown in Fig. 7(b), the Cu7.5 alloy demonstrates a stable elastocaloric response over 200 tensile loading–unloading cycles, with nearly unchanged ΔT_{ad}, indicating great potential for practical applications. Although increasing Cu content improves lattice compatibility between the transforming phases, it simultaneously reduces the enthalpy change ΔH associated with the B2 ↔ B19 (B19′) transformation, and therefore excessive Cu doping is undesirable.[29] The great comprehensive performance at room temperature is achieved through a synergistic strategy involving Co doping, which slightly lowers the transformation temperature, and the optimal selection of 7.5 at.% Cu content, which effectively balances phase stability with functional properties.

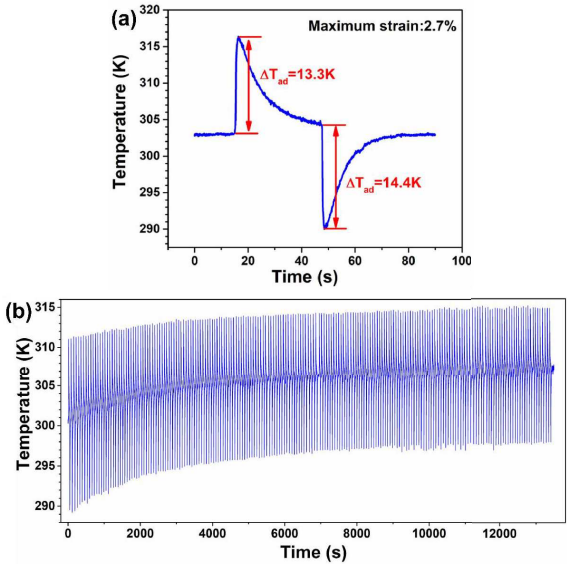


Fig. 7. (a) Temperature variation during loading with a strain rate of 5.6×10^{-2} s^{-1} to amaximum strain of 2.7%, holding, unloading with a strain rate of 9×10^{-2} s^{-1}, and further holding, as a function of time. (b) Temperature variation during 200 cycles of loading, holding, unloading and further holding, shown as a function of time. The maximum strain is 2.2%. The loading and unloading rates are 5.6×10^{-2} s^{-1} and 9×10^{-2} s^{-1}, respectively. Adapted from Ref. [29].

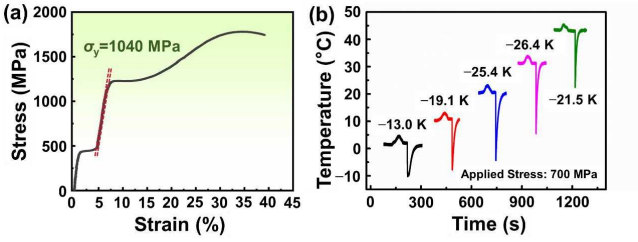


Fig. 8. (a) Compressive stress–strain curve of the $Ti_{48.5}Ni_{46.5}Ga_5$ alloy during loading until fracture. σ_y represents the yield strength of the alloy. (b) Temperature variations as a function of time recorded during elastocaloric effect measurements under different ambient temperatures at a constant σ_{max} of 700 MPa. Adapted from Ref. [42].

Additionally, Kim *et al.*[69] introduced V as a ternary alloying element into equiatomic Ni–Ti SMAs. The V con-

tent was delicately optimized to achieve transformation temperatures slightly below room temperature ($A_f = 288$ K) and a low thermal hysteresis of 12 K. The $Ni_{50}Ti_{45.3}V_{4.7}$ alloy demonstrates a reversible ΔT_{ad} of 12.5 K under a compressive stress of 260 MPa at room temperature, with no significant degradation in the elastocaloric effect after 5000 loading-unloading cycles. Upon unloading from 170 MPa, the alloy achieves a high $\Delta T_{ad}/\sigma$ value of 51.5 K·GPa^{-1} and a $COP_{ReverseBrayton}$ of 22.5. Wang *et al.*[42] reported that a bulk polycrystalline $Ti_{48.5}Ni_{46.5}Ga_5$ alloy, fabricated via simple casting and solution treatment, exhibits a large ΔT_{ad} of 24.8 K and a high $\Delta T_{ad}/\sigma$ value of 49.6 K·GPa^{-1} upon unloading from 500 MPa at room temperature. The high yield strength of $\sim$ 1140 MPa (Fig. 8(a)), which exceeds that of conventional coarse-grained binary Ni–Ti SMAs, is attributed to lattice distortion and localized strain fields resulting from Ga substitution. Meanwhile, the relatively low driving force ($\sim$ 405 MPa) required for stress-induced martensitic transformation, combined with a narrow stress hysteresis of 98 MPa, contributes to enhanced phase transformation reversibility and improved stability of the elastocaloric effect.[42] As shown in Fig. 8(b), the $Ti_{48.5}Ni_{46.5}Ga_5$ alloy demonstrates an effective operating temperature range from 273 K to 323 K, highlighting its promising potential for practical near-room-temperature refrigeration applications. Aaltio *et al.*[66] suppressed the stress-induced B2 $\rightarrow$ B19′ transformation by substituting Ni with Fe, thereby avoiding the large stress hysteresis and high energy dissipation associated with this phase transition. Instead, the B2 $\rightarrow$ R transformation, which exhibits lower energy dissipation, was achieved. The maximum ΔT_{ad} estimated from the latent heat ΔH of the R $\rightarrow$ B2 transformation reaches 12.4 K for the $Ni_{48}Ti_{50}Fe_2$ alloy and 8.7 K for the $Ni_{46}Ti_{50}Fe_4$ alloy.

Introducing nanocomposite microstructures or coherent precipitates into the matrix can significantly improve the stability of the elastocaloric effect, maintaining high functional performance over millions of cycles without substantial degradation. Hou *et al.*[32] leveraged the localized molten environment and near-eutectic mixing of elemental powders inherent in the powder-feed laser-directed-energy deposition (L-DED) additive manufacturing process to facilitate the formation of Ni-rich, non-transforming intermetallic compounds (Ni_3Ti phases). These phases exhibit intricate dendritic morphologies and are uniformly dispersed within a binary Ni–Ti matrix at high volume fractions (up to 50 vol.%), thereby contributing to improved functional stability. As a result, the L-DED-produced nanocomposite exhibits quasi-linear superelasticity, which was attributed by the authors to effective load transfer between the intermetallic Ni_3Ti phase and the binary matrix phase.[70,71] A ΔT_{ad} of 4.1 K is obtained upon unloading from a large applied stress of approximately 1400 MPa at room temperature. Furthermore, both the mechanical response and elastocaloric effect exhibit remarkable stability for more than one million cycles, highlighting its promise for commercial solid-state refrigeration applications.[32] This outstanding cyclic stability is enabled by the dendritic Ni_3Ti reinforcements, which contribute to a small hysteresis and thereby effectively mitigate material fatigue and failure. It is worth noting that, despite the exceptional cyclic stability, the magnitude of ΔT_{ad} was greatly reduced due to the presence of a high fraction of non-transforming Ni_3Ti phase.

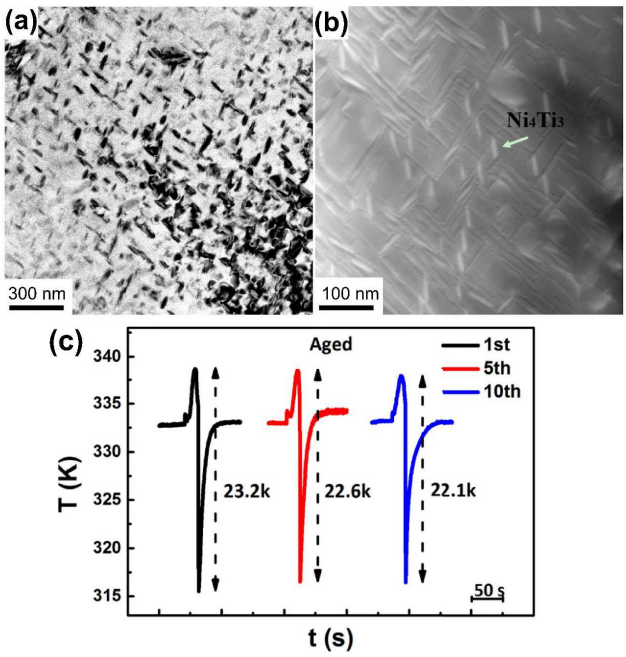


Fig. 9. (a) TEM bright field image of the aged $Ni_{51.4}Ti_{48.6}$ 3D-printed alloy. (b) High-angle annular dark field scanning transmission electron microscopy (HAADF-STEM) image of the aged $Ni_{51.4}Ti_{48.6}$ 3D-printed alloy. (c) Temperature variation during the 1st, 5th and 10th cycles of loading (with a strain rate of 10^{-3} s^{-1}), unloading (with a strain rate of 6 s^{-1}), and holding, shown as a function of time for the aged $Ni_{51.4}Ti_{48.6}$ 3D-printed alloy. Adapted from Ref. [72].

Cao *et al.*[72] fabricated a $Ni_{51.4}Ti_{48.6}$ alloy using the selective laser melting (SLM) additive manufacturing technique. The functional performance and transformation temperature of the 3D-printed alloy can be effectively tuned by adjusting SLM processing parameters and applying post-process heat treatments. As shown in Figs. 9(a) and 9(b), the TEM bright-field images of the 3D-printed binary alloy produced with a hatch spacing (h_s) of 0.08 mm reveal randomly distributed nanoscale Ni_4Ti_3 precipitates, less than 80 nm in size, within the matrix after ageing treatment at 723 K for 5 h. Consequently, the aged alloy exhibits a significantly enhanced elastocaloric effect, achieving a ΔT_{ad} of up to 23.2 K upon unloading from a compressive stress of 750 MPa at 333 K (Fig. 9(c)).[72] Moreover, the combined effects of pronounced precipitate hardening and low stress hysteresis result in a stable superelastic response, maintaining complete strain recovery over 10 cycles. Notably, the aged alloy exhibits excellent

cyclic stability of the elastocaloric effect, with less than 5% degradation in ΔT_{ad} after the same number of stress cycles.

More recently, Lin *et al.*[73] developed a bulk $Ti_{49.2}Ni_{42.3}Cu_{7.5}Co_1$ alloy that achieved a large-yet-stable elastocaloric cooling property through combining an ageing treatment with premultiaxial forging (MAF) after the homogenization process. Specifically, the selection of the intermediate 7.5 at.% Cu content maintained the B2 $\rightarrow$ B19′ transformation with a relatively large ΔT_{ad}. On the other hand, uniformly distributed nanoscale coherent Ti(Ni, Cu)$_2$ precipitates (Fig. 10(a)) formed in the alloy, which significantly enhances the yield strength and thus suppresses dislocation motion during the cyclic phase transition. As a result, the bulk Ti–Ni–Cu–Co alloy exhibited a high yield strength (1804 MPa, as shown in Fig. 10(b)) and a low critical stress for martensitic transformation (350 MPa). Moreover, stable cyclic stress–strain responses were achieved under a compressive stress of 550 MPa for over 1×10^8 cycles (Fig. 10(c)). Notably, the significant disparity between the yield strength and the externally applied stress can contribute to the effective inhibition of dislocation motion. Additionally, it exhibited a large and stable ΔT_{ad} (up to 17 K, as shown in Fig. 1(d)) and a high $\Delta T_{ad}/\sigma$ (31 K·GPa^{-1}) during these cycles.

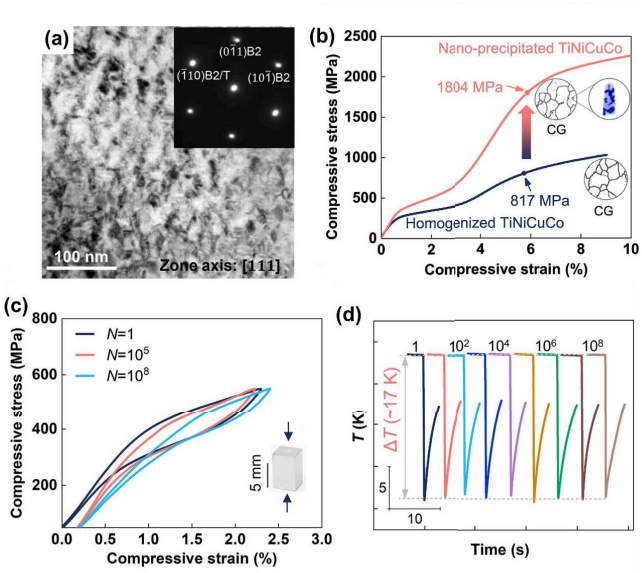


Fig. 10. (a) Bright-field TEM image with corresponding selected area diffraction pattern (SADP), where B2 and T represent the lattice structures of austenite phase and tetragonal Ti(Ni, Cu)$_2$ nanoprecipitate, respectively. (b) Large-strain compressive stress–strain curves showing enhancement in yield stress of the nano-precipitated Ti–Ni–Cu–Co compared to an as-homogenized Ti–Ni–Cu–Co (coarse grain without nanoprecipitates). Both tests in panel (b) were performed at the temperatures of $A_f + 10$ K, that is, 297 K (room temperature) and 223 K for the nanoprecipitated and the homogenized TiNiCuCo, respectively. Cyclic compressive quasistatic stress–strain responses (a) and ΔT_{ad} (b) over 1×10^8 phase-transition cycles of the nano-precipitated Ti–Ni–Cu–Co at room temperature. Adapted from Ref. [73].

Refining grains through complex cold/hot deformation processes can effectively suppress dislocation motion and enhance the yield strength of alloys, thereby improving their cyclic stability under stress cycling. Similarly, researchers have also intensively focused on the elastocaloric effect and fatigue lifetime in nanocrystalline Ni–Ti-based alloys. As grain size decreases, the volume fraction of grain boundaries increases, leading to a monotonic reduction in the elastocaloric effect. Furthermore, the phase transformation tends to evolve into a continuous, stable, and reversible process, in contrast to the conventional nucleation-and-growth mechanism observed in coarse-grained polycrystals. This evolution is attributed to the constraints imposed by grain boundaries in nanocrystalline alloys, where phase transformations occur within extremely confined spatial regions. As a result, the stress–strain behavior of nanocrystalline Ni–Ti-based alloys increasingly approaches ideal reversible elasticity, exhibiting small stress hysteresis and reduced temperature dependence. Notably, stress-induced martensitic transformation can be fully suppressed when the grain size is refined below 60 nm.[70]

Zhou *et al.*[74] systematically investigated the grain-size effect on the elastocaloric effect and its reversibility in nanograined Ni–Ti alloys fabricated through cold rolling and annealing. It was revealed that reducing the grain size to the nanoscale (average grain size $\sim$ 4 nm) significantly improved superelasticity, achieving a large reversible strain of 5% with a small stress hysteresis. Meanwhile, the very low stress hysteresis greatly reduces the friction dissipation associated with martensitic transformation, resulting in excellent elastocaloric reversibility and high energy conversion efficiency of the elastocaloric effect. As a result, the ΔT_{ad} value ($\sim$ 9 K) upon loading was almost equal to that upon unloading when the applied strain was 3%. However, as the annealing temperature increases and the holding time extends, coarser grains lead to the degradation of superelastic responses, resulting in an increase in residual strain and stress hysteresis loop.

Chen *et al.*[75] investigated the functional stability and structural fatigue behavior of polycrystalline $Ni_{50.6}Ti_{49.4}$ cylinders with an average grain size of 100 nm under cyclic compression at a frequency of 20 Hz and a maximum stress of 800 MPa. Notably, the cylinders achieved a fatigue life of approximately 70 million cycles. After 65 million cycles, the nanocrystalline cylinder demonstrated a ΔT_{ad} of 9.9 K and a $COP_{ReverseBrayton}$ of 18.8 at an ambient temperature of 303 K. Lin *et al.*[76] combined grain refinement and high-density dislocations to enhance the cyclic stability of Ni–Ti alloys. The nanocrystalline $Ni_{50.8}Ti_{49.2}$ alloy was fabricated through cold rolling followed by low-temperature annealing (583 K, 2 min), yielding an average grain size of 31 nm and high-density dislocation cells with diameters of 15 nm. Consequently, the room-temperature yield strength of this high-density dislocation nanocrystalline (HDDN) $Ni_{50.8}Ti_{49.2}$ alloy reaches 2090 MPa, which can be attributed to the synergistic strengthening effects arising from grain boundary strengthening, governed by

the Hall–Petch relationship, and dislocation strengthening, described by Taylor hardening theory.[77,78] More importantly, the HDDN $Ni_{50.8}Ti_{49.2}$ exhibits a stable room-temperature temperature change of 17.3 K over one million transformation cycles under a high compressive stress of 1400 MPa, demonstrating its potential for long-term elastocaloric cooling applications.

Liang *et al.*[79] reported that nanocrystalline $Ni_{50.57}Ti_{49.43}$ tubes fabricated by cold drawing exhibit lenticular grains with a thickness of 78 nm, demonstrating superior fatigue resistance, sustaining over 120 million cycles under a compressive stress of 800 MPa at a frequency of 20 Hz in air. The ΔT_{ad} during unloading shows good cyclic stability, decreasing slightly from an initial value of 7.0 K to 6.6 K after 120 million cycles.[79] Meanwhile, the $COP_{ReverseBrayton}$ increases from an initial value of 8.8 to 11.6 after 100 million compressive cycles. Consequently, these Ni–Ti tubes demonstrate both a stable elastocaloric effect and an ultrahigh fatigue lifetime. Wang *et al.*[80] introduced near-saturated dislocation structures and residual martensite nanodomains into the B2 matrix through overstress training, i.e., applying five loading cycles at a maximum stress of 1900 MPa — significantly exceeding the yield strength of cold-drawn and annealed nanocrystalline Ni–Ti tubes. As a result, the microstructure of the trained tube exhibits a high density of dislocations that aggregate to subdivide the B2 matrix into fine nanodomains with diameters of 5–10 nm. This dislocation-rich nanostructure effectively suppresses further dislocation formation and motion during subsequent cyclic compression, thereby substantially improving the cyclic stability of the Ni–Ti tube. Consequently, the trained Ni–Ti tube maintains a stable ΔT_{ad} of 11 K after one million compressive cycles under 1000 MPa at a frequency of 10 Hz at room temperature.[80] It is worth mentioning that Ni–Ti tubes and tubular structures, which offer high heat transfer rates, are regarded as among the most promising configurations for elastocaloric refrigeration.

Recently, Chen *et al.*[36,81–83] reported a series of gradient-structured (GS) $Ni_{50.8}Ti_{49.2}$ alloys fabricated by applying various precisely controlled laser surface annealing processes to a severely deformed cold-rolled sheet. The strong synergetic interaction between fine-grained and coarse-grained layers enables highly tunable mechanical properties and a significantly enhanced elastocaloric response in these GS alloys. Specifically, the fine-grained layers bear higher loads and promote transformation homogenization, leading to lower energy dissipation, whereas the coarser-grained layers contribute more effectively to a stronger elastocaloric effect. Consequently, the unique superelastic response of the GS Ni–Ti alloys differs markedly from that of the initial cold-rolled sheet, which exhibits a quasi-linear superelastic response, as well as from that of coarse-grained Ni–Ti, which shows a typical stress plateau accompanied by a large hysteresis loop. The elastocaloric cooling performance of GS Ni–Ti was evaluated, demonstrating a ΔT_{ad} of 9.4 K under a maximum tensile strain of 3.5% at room temperature.[83] Moreover, GS Ni–Ti exhibits low stress hysteresis, high yield strength, and excellent mechanical compatibility across heterogeneous domains; these characteristics collectively enhance long-term cyclic stability and enable an expanded working temperature range for elastocaloric cooling applications. Dang *et al.*[84] developed several ternary Ti–Ni–Cu alloys manufactured via cold rolling followed by heat treatment. The cold-rolled and annealed nanocrystalline $Ti_{50}Ni_{40}Cu_{10}$ alloy exhibits a large ΔT_{ad} exceeding 20 K when tested at a relatively high temperature of 340 K, with no significant degradation observed over 200 tensile cycles. Furthermore, Dang *et al.*[85] developed a bulk ternary aged nanocrystalline (ANC) $Ni_{40.8}Ti_{49.2}Cu_{10}$ alloy by combining cold rolling with subsequent ageing treatment. The novel ANC alloy exhibits a ΔT_{ad} of 13.8 K with only 0.3 K degradation after 450 tensile cycles at room temperature (Fig. 11). This remarkable elastocaloric performance can be attributed to the synergistic strengthening effect between the nanocrystallinity induced by cold rolling and the uniformly distributed coherent $Ti(Ni, Cu)_2$ nanoprecipitates formed during ageing.[85] Specifically, the high-density dislocation networks introduced by cold rolling increase the critical stress for dislocation slip, thereby suppressing plastic deformation. Simultaneously, these dislocations act as nucleation sites for precipitates and accelerate the precipitation process, collectively enhancing the reversibility of the B2 ↔ B19 transformation and inhibiting dislocation accumulation during cyclic loading.

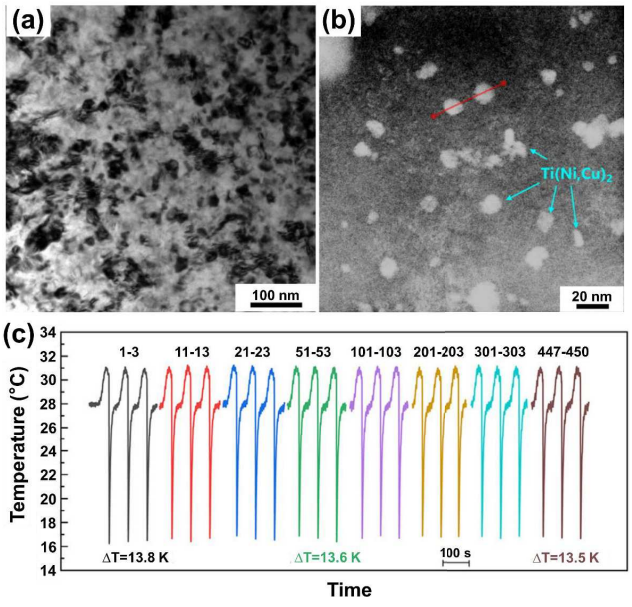


Fig. 11. (a) Bright field image of the ageing nanocrystalline (ANC) $Ni_{40.8}Ti_{49.2}Cu_{10}$ alloy. (b) HAADF-STEM image of the ANC alloy showing spherical nanoprecipitates. (c) The ΔT_{ad} of the ANC alloy as a function of cycling number. Adapted from Ref. [85].

High entropy alloys (HEAs), typically defined as alloys containing at least five principal elements with the concentration of each element ranging from 5 at.% to 35 at.%, can exhibit desirable properties such as high strength, excellent ductility, and superior wear resistance. The concept of HEAs presents a promising strategy for addressing the limitations of conventional Ni–Ti SMAs, particularly their poor cyclic stability and narrow operational temperature range for the elastocaloric effect. The significant lattice distortion inherent in HEAs leads to pronounced solid solution hardening, while the sluggish diffusion kinetics does not hinder martensitic transformation, thus preserving the functional properties essential for elastocaloric applications. Moreover, the high yield strength of HEAs enables a broader temperature range for stress-induced martensitic transformation. Li *et al.*[86] reported a $NiCuTiHf_{0.6}Zr_{0.4}$ high entropy SMA with a yield strength exceeding 1.7 GPa, which exhibits a large ΔT_{ad} of 9.3 K over a broad temperature range from 303 K to 423 K. Subsequently, Liu *et al.*[87] developed a $Ti_{31}Zr_5Hf_{14}Ni_{32}Co_4Cu_{14}$ high entropy SMA that demonstrates a stable elastocaloric effect, achieving a ΔT_{ad} of 11.5 K after 10000 compressive stress cycles at room temperature (297 K).

As mentioned above, numerous studies have been conducted on elastocaloric cooling based on Ni–Ti-based SMAs. To clearly illustrate the advantages of the aforementioned Ni–Ti-based elastocaloric materials for cooling applications, we compared multiple properties of typical alloys using radar charts. Notably, the fatigue performance of elastocaloric materials exhibits significant differences under different loading modes. Therefore, Figs. 12(a) and 12(b) show the property comparison under compressive and tensile loading, respectively. Overall, the Ni–Ti-based SMAs demonstrate comprehensive advantages for elastocaloric cooling applications under compressive loading.

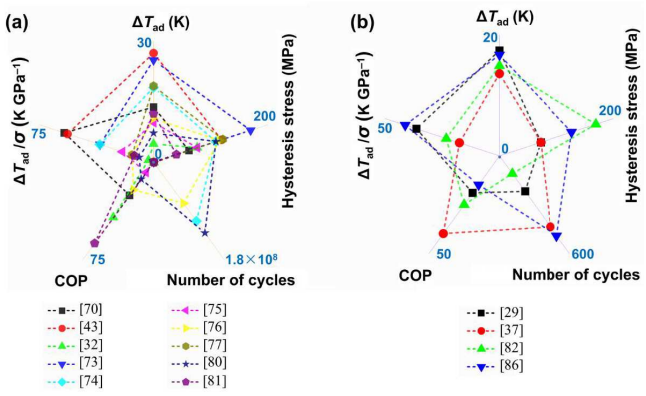


Fig. 12. Comprehensive comparison of multiple properties of Ni–Ti-based SMAs under different loading modes. (a) Compressive mode. (b) Tensile mode.

4. Other types of elastocaloric alloys

Co–V–Ga Heusler-type SMAs, which undergo a martensitic transformation from a $L2_1$ cubic phase to the $D0_{22}$ tetragonal phase accompanied by a considerable entropy change, have demonstrated great promise for elastocaloric refrigeration applications over a wide operational temperature range.[88,89] Niu *et al.*[30] reported a [001]-oriented $Co_{50.7}V_{33.3}Ga_{16}$ alloy fabricated by directional solidification, achieving a large ΔT_{ad} of 18.7 K during unloading from a uniaxial compressive stress of 400 MPa at 297 K. Surprisingly, this alloy exhibits good cyclic stability without observable degradation in the elastocaloric effect after 100 cycles. Moreover, a large ΔT_{ad} of approximately 12.5 K was maintained across a broad temperature range (258–373 K). Liu *et al.*[90] developed a polycrystalline $Co_{50}V_{35}Ga_{14}Ni_1$ alloy, achieving a large ΔT_{ad} of 12.1 K upon unloading. This alloy also demonstrates good cyclic stability, retaining its elastocaloric performance over 4000 loading–unloading cycles without significant degradation. Niu *et al.*[91] engineered a promising $Co_{47}V_{29}Ti_{22.5}Fe_{1.5}$ alloy through a combination of a two-step martensitic transformation pathway with an all-d-metal design. This alloy exhibits a large ΔT_{ad} of 24 K and a $COP_{ReverseBrayton}$ of 25 upon rapid removal of a maximum stress of 900 MPa at room temperature. More impressively, a stable ΔT_{ad} of 23.5 K was still maintained after 10000 cycles. Co–Ni–Ga SMAs, a class of CsCl-type B2 intermetallic compounds, have attracted attention for elastocaloric refrigeration due to their narrow stress hysteresis, low transformation driving force, and broad operating temperature range.[92,93] Zhang *et al.*[94] fabricated a polycrystalline $(Co_{47.1}Ni_{22.9}Ga_{30})_{96}Cu_{3.8}B_{0.2}$ alloy with a $\langle 001\rangle_{B2}$ texture and ductile secondary phases. This textured heterostructural alloy demonstrates a stable room-temperature elastocaloric effect, with a ΔT_{ad} of 3.2 K upon unloading and no observable degradation after 20000 cycles.

Ni–Fe–Ga-based SMAs seem attractive for elastocaloric refrigeration due to their low critical stress for martensitic transformation (typically < 100 MPa).[95,96] However, single-phase polycrystalline Ni–Fe–Ga alloys suffer from poor cyclic stability, failing after just 10 cycles due to intergranular cracking. Notably, single crystalline Ni–Fe–Ga-based SMAs demonstrate good cyclability under repeated stress cycles. Li *et al.*[97] developed a [420]-oriented $Ni_{54}Fe_{19}Ga_{27}$ single crystal fabricated using the float-zone-melting technique. This alloy exhibited a suitable A_f of 284.3 K, a reversible temperature change of 7.5 K at 3.8% transformation strain under a relatively low driving stress of approximately 30 MPa, and a corresponding exceptional $\Delta T_{ad}/\sigma$ of 250 K·GPa^{-1} at 293 K. Pataky *et al.*[20,98] reported a single-crystal Ni_2FeGa alloy which demonstrated a large ΔT_{ad} of 13.5 K with high cyclic stability over 10^4 cycles. However, it is worth noting that the

testing temperature ($\sim$ 323 K) far exceeds the desirable room-temperature requirements. Additionally, single-crystal Ni–Fe–Ga-based SMAs also face limitations such as severe chemical segregation, slow growth rates, and high production costs. Imran *et al.*[99] investigated the elastocaloric effect and cyclic stability of porous $Ni_{53.5}Fe_{19.9}Ga_{26.6}$ foams (53% porosity) and the bulk counterpart $Ni_{53}Fe_{19.4}Ga_{27.6}$ alloy. The porous structure of the foams mitigates the constraints of grain boundaries and reduces the stress hysteresis during cyclic loading. Consequently, although the foams exhibit a lower ΔT_{ad} of 2.8 K compared to 5.8 K for the bulk counterpart, they demonstrate better cyclic stability over 100 cycles relative to the bulk counterpart. Furthermore, Imran *et al.*[100] also reported Ni–Fe–Ga foams with a stable ΔT_{ad} of 4.1 K, a high $\Delta T_{ad}/\sigma$ value of 58.6 K·GPa^{-1}, and a $COP_{ReverseBrayton}$ of 22 under a low stress of 70 MPa for 194 cycles. Huang *et al.*[101] introduced a microstructure design strategy combining strong texture (to reduce strain incompatibility) with a ductile interfacial γ-phase (to prevent intergranular fracture) to improve mechanical properties, thereby enhancing the cyclability of the elastocaloric effect in Ni–Fe–Ga alloys. Their polycrystalline $Ni_{54}Fe_{19}Ga_{27}$ alloys, fabricated by directional solidification and a subsequent annealing process, exhibit a compressive strength of 1.5 GPa at room temperature. A ΔT_{ad} of 8.5 K was obtained under 6% strain at 318 K.[101] Furthermore, a stable ΔT_{ad} of $\sim$ 3 K was maintained over 20000 cycles without appreciable degradation, which demonstrates good cyclability for the polycrystalline Ni–Fe–Ga alloys.

As promising elastocaloric materials, Cu-based SMAs exhibit notable advantages such as low cost, high thermal conductivity, small stress hysteresis, and a wide operating temperature range.[102,103] Qian *et al.*[104] reported a ΔT_{ad} of 4.0 K for the $Cu_{68}Al_{16}Zn_{14}$ alloy and 3.9 K for the $Cu_{73}Al_{15}Mn_{12}$ alloy under compressive loading. Moreover, Cu–Al–Mn single crystals can be easily fabricated using the abnormal grain growth (AGG) enabled by simple cyclic heat treatments,[105,106] which can efficiently eliminate the intergranular constraints and suppress plastic slip during stress-induced martensitic transformation. Lu *et al.*[107] developed an AGG-processed bicrystalline $Cu_{71}Al_{17}Mn_{12}$ alloy with a low A_f of 202 K, achieving a ΔT_{ad} of 6.5 K at room temperature. Wang *et al.*[108] developed a $\langle 105\rangle_A$-oriented $Cu_{68.5}Al_{17.5}Mn_{14}$ single crystal that shows a ΔT_{ad} of 6.6 K during rapid removal of 10% strain at 290 K. The cyclability of the elastocaloric effect was examined under cyclic compressive loading with a maximum compressive strain of 8%. After 6000 cycles, the ΔT_{ad} decreased from 6.5 K to 3.5 K, attributed to the accumulation of lattice defects. Moreover, the $Cu_{68.5}Al_{17.5}Mn_{14}$ alloy exhibits a wide working temperature range, spanning from 77 K to 450 K. Guo *et al.*[109] reported a $Cu_{68.7}Al_{17.9}Mn_{13.4}$ single crystal fabricated by directional solidification and subsequent AGG process, which exhibits a ΔT_{ad} of 10.2 K upon unloading at 290 K and a broad operating temperature window ranging from 140 K to 410 K. Furthermore, Fan *et al.*[110] achieved a large ΔT_{ad} of 19.5 K upon unloading in [001]-oriented $Cu_{71}Al_{17.5}Mn_{11.5}$ single crystals produced by high-rate directional solidification and subsequent AGG process. After 10000 cycles with a maximum uniaxial compressive stress of 350 MPa, no obvious cracks were observed on the sample surface. However, the corresponding ΔT_{ad} significantly decreased from 19.5 K to 2.1 K, which was attributed to the accumulation of a high density of dislocations and residual martensite during cyclic loading. Li *et al.*[111] reported a columnar-grained $Cu_{71}Al_{17.5}Mn_{11.5}$ alloy with a strong $\langle 001\rangle$ texture, fabricated using the laser-based powder bed fusion of metals (PBF–LB/M) technique, showing a ΔT_{ad} of 8.0 K upon unloading at room temperature.

Notably, Li *et al.*[112] proposed a novel non-phase-transition-based approach to achieve highly efficient solid-state heat pumping by utilizing the thermoelastic effect based on the linear elastic deformation in the martensitic phase of ferroelastic alloys. The thermoelastic effect is closely associated with the intrinsic linear coefficient of thermal expansion (CTE) along the loading direction, which shows significant anisotropy among the crystallographic directions. Specifically, [001]-textured $Ti_{78}Nb_{22}$ martensitic polycrystals were fabricated through a two-step plastic deformation process involving cold rolling and compression (CRC). The alloy exhibits no discernible martensite–austenite transition driven by thermal or stress fields. It exhibits near-linear stress–strain curves with a practically zero hysteresis loop area within the wide temperature range of 298–473 K. Meanwhile, upon the rapid release of a 700 MPa stress, a ΔT_{ad} of approximately 2.2 K is observed at 298 K, and the ΔT_{ad} reaches 5.2 K at 473 K. The increased ΔT_{ad} values can be attributed to the elevation of the CTE as the ambient temperature rises. These ΔT_{ad} values are far higher than the ΔT_{ad} values of conventional metallic materials, polymers, glass, and ceramics. The non-phase-transition [001]-textured $Ti_{78}Nb_{22}$ demonstrates a $COP_{ReverseStirling}$ of 25.3, which significantly surpasses those associated with typical first-order phase transitions in elastocaloric SMAs. Additionally, cyclic stability over 10 million cycles is also achieved under a compressive stress of 700 MPa at 298 K. It is worth mentioning that, in addition to solid-state heat pumping, this highly efficient non-phase-transition-based strategy for caloric effect can serve as excellent guidance for the material exploration of elastocaloric refrigeration.

Next, we compared multiple properties of different types of SMAs using a radar chart (Fig. 13). Obviously, those elastocaloric materials based on the first-order martensitic transformation are typically limited by poor fatigue resistance. However, the $Ti_{78}Nb_{22}$ alloy, which operates based on the ther-

moelastic effect associated with thermal expansion, shows an outstanding fatigue life. Nevertheless, its ΔT_{ad} value is inadequate. Therefore, considerable research efforts are still required to optimize their overall elastocaloric performance.

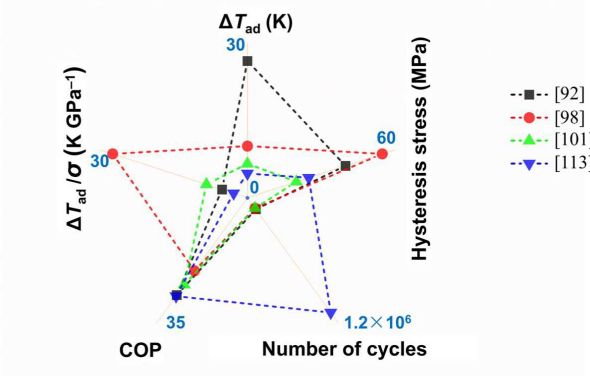


Fig. 13. Comprehensive comparison of multiple properties of different types of SMAs introduced in Section 4.

5. Summary and outlook

Highly efficient and environmentally friendly elastocaloric refrigeration, which leverages the thermal effect associated with stress-induced martensitic transformation in elastocaloric materials, has attracted significant attention as a promising solid-state alternative to conventional vapor-compression refrigeration technology, which exacerbates the global warming crisis. The performance of elastocaloric refrigeration systems depends critically on the properties of the elastocaloric materials, which serve as the solid-state refrigerants. Ideal elastocaloric materials are expected to simultaneously meet several critical criteria: (a) large latent heat, (b) excellent functional fatigue resistance, (c) an appropriate and broad operational temperature window, (d) robust mechanical properties, (e) low stress hysteresis, (f) high COP, and (g) cost-effectiveness. In this paper, we present an overview of recent advancements in various types of SMAs for elastocaloric refrigeration, with a focus on Ni–Mn-based, Ni–Ti-based, Co-based, Ni–Fe–Ga-based, and Cu-based alloys. This review systematically evaluates their elastocaloric performance, underlying microstructural mechanisms, and persisting challenges limiting their practical implementation. Current strategies to improve elastocaloric performance primarily involve: (a) compositional design to improve crystallographic compatibility between transforming phases and to tailor phase transformation temperatures, (b) texture engineering via advanced processing techniques such as directional solidification, and (c) strengthening approaches such as grain refinement and precipitation hardening.

While remarkable progress has been made in boosting the elastocaloric effect, these advancements unfortunately often come at the expense of other important material properties, posing a major obstacle to practical application. Although Ni–Mn-based alloys have recently been demonstrated to show very large values of ΔT_{ad} exceeding 30 K, their intrinsic brittleness and unsatisfactory fatigue resistance still require improvement in future work. As the leading candidate among SMAs for elastocaloric refrigeration, Ni–Ti-based alloys demonstrate excellent cyclic stability of the elastocaloric effect, maintaining a moderate elastocaloric effect on the order of one million cycles through various optimized strategies reported in the literature. However, their practical application in refrigeration is still restricted by a limited ΔT_{ad}, a large driving force, and an unsuitable working temperature range. Other types of elastocaloric alloys, including Co-based, Ni–Fe–Ga-based, and Cu-based SMAs, often suffer from unsatisfactory mechanical properties, inadequate functional durability, and high cost, which inhibit their widespread use in elastocaloric refrigeration.

To overcome these limitations, emerging methodologies such as multiscale simulations, machine learning-aided design, and novel manufacturing techniques are being leveraged to develop next-generation elastocaloric materials. We anticipate that through the synergistic combination of advanced materials design strategies and novel fabrication technologies, high-performance elastocaloric materials will be developed and sustainable eco-friendly elastocaloric refrigeration will achieve widespread adoption in diverse industrial and domestic applications in the near future.

Acknowledgments

Project supported by the National Natural Science Foundation of China (Grant Nos. 52325101, 52171172, and 52031005), the Fundamental Research Funds for the Central Universities (Grant No. FRF-TP-24-01C), the State Key Laboratory for Advanced Metals and Materials (Grant No. 2025-Z32), the Science and Technology Innovation Program of Hunan Province (Grant No. 2023RC4009), and Hunan Provincial Natural Science Foundation of China (Grant No. 2023JJ30190).

References

[1] Xiao F, Chen H and Jin X J 2021 *Acta Metal. Sin.* **57** 1
[2] Qian S X, Catalini D, Muehlbauer J, Liu B Y, Mevada H, Hou H L, Hwang Y H, Radermacher R and Takeuchi I 2023 *Science* **380** 722
[3] Li L J, He S Y, Xiao F, Zeng Y, Liu Y, Zhou Y, Cai X R and Jin X J 2025 *Prog. Mater. Sci.* **153** 101477
[4] Chen J Y, Lei L P and Fang G 2021 *Mater. Today Commun.* **28** 102706
[5] Zuo C D, Zheng L J, Yang S C, Li B and Zhang H 2024 *Next Mater.* **5** 100270
[6] Zheng S Y, Du F H, Zheng L R, Han D L, Li Q, Shi J Y, Chen J P, Shi X M, Huang H B, Luo Y R, Yang Y R, O'Reilly P, Wei L L, de Souza N, Hong L and Qian X S 2023 *Science* **382** 1020
[7] Tishin A M and Spichkin Y I 2014 *IIR* **37** 223
[8] Bonnot E, Romero R, Manosa L, Vives E and Planes A 2008 *Phys. Rev. Lett.* **100** 125901
[9] Aznar A, Lloveras P, Kim J Y, Stern-Taulats E, Barrio M, Tamarit J L, Sánchez-Valds C F, Llamazares J L S, Mathur N D and Moya X 2019 *Adv. Mater.* **31** 1903577
[10] Gong J, Chu S R, Mehta R K and McGaughey A J H 2022 *npj Comput. Mater.* **8** 140

[11] Zhang S, Deliyore-Ramirez J, Deng S, Nair B, Pesquera D, Jing Q, Vickers M E, Crossley S, Ghidini M, Kar-Narayan S, Guzmán-Verri G G, Moya X and Mathur N D 2024 *Nat. Mater.* **23** 639
[12] Xu X, Li M, Lin X and Wang H 2024 *Phys. Rev. B* **110** 064103
[13] Du F H, Yang T N, Hao H, *et al.* 2025 *Nature* **640** 924
[14] Xu X, Xie W F, Li F B, Niu C, Li M and Wang H 2024 *Phys. Rev. Appl.* **22** 014036
[15] Li B, Kawakita Y, Wang H, Kikuchi T, Yu D H, Yano S, Ren W J, Nakajima K and Zhang Z D 2019 *Nature* **567** 506
[16] Li F B, Li M, Niu C and Wang H 2022 *Appl. Phys. Lett.* **120** 073902
[17] Piper S L, Melag L, Kar M, Sourjah A, Xiao X, May E F, Aguey-Zinsou K F, MacFarlane D R and Pringle J M 2025 *Science* **387** 56
[18] Cheng P T, Chen Z H, Zhang C L, Zhang Z M, Li B and Wang D H 2025 *Chin. Phys. B* **34** 036801
[19] Energy savings potential and RD&D opportunities for Non-Vapor-Compression HVAC technologies, March 2014 Report of the U.S. Dpt. of Energy.
[20] Wu Y, Ertekin E and Sehitoglu H 2017 *Acta Mater.* **135** 158
[21] Chen Y, Zhang X X, Dunand D C and Schul C A 2009 *Appl. Phys. Lett.* **95** 171906
[22] Cong D Y, Xiong W X, Planes A, Ren Y, Manosa L, Cao P Y, Nie Z H, Sun X M, Yang Z, Hong X F and Wang Y D 2019 *Phys. Rev. Lett.* **122** 255703
[23] Yang Z, Cong D Y, Yuan Y, Wu Y, Nie Z H, Li R G and Wang Y D 2019 *Mate. Res. Lett.* **7** 137
[24] Guan Z Q, Bai J, Sun S D, Gu J L, Liang X Z, Zhang Y D, Esling C, Zhao X and Zuo L 2022 *Appl. Mater. Today* **29** 101634
[25] Zhang X Y, Qian H Y, Cai R, Wei Z Y, He J, Zhang M X, Sun W, Liu J, Felser C and Li G W 2024 *ACS Appl. Electron. Mater.* **6** 4440
[26] Omori T, Iwaizako H and Kainuma R 2016 *Mater. Des.* **101** 263
[27] Kirsch S M, Welsch F, Michaelis N, Schmidt M, Wieczorek A, Frenzel J, Eggeler G, Schütze A and Seelecke S 2018 *Energy Technol.* **6** 1567
[28] Mañosa L and Planes A 2016 *Philos. T. R. Soc. A* **374** 20150310
[29] Yang Z, Cong D Y, Yuan Y, Li R G, Zheng H X, Sun X M, Nie Z H, Ren Y and Wang Y D 2020 *Appl. Mater. Today* **21** 100844
[30] Niu Y R, Chen H Y, Zhang X Y, Li S W, Cong D Y, Ma T Y, Li S L, Lin J P and Wang Y D 2021 *Scr. Mater.* **204** 114123
[31] Mañosa L and Planes A 2017 *Adv. Mater.* **29** 1603607
[32] Hou H L, Simsek E, Ma T, Johnson N S, Qian S X, Cissé C, Stasak D, Al Hasan N, Zhou L, Hwang Y H, Radermacher R, Levitas V I, Kramer M J, Zaeem M A, Stebner A P, Ott R T, Cui J and Takeuchi I 2019 *Science* **366** 1116
[33] Moya X, Kar-Narayan S and Mathur N D 2014 *Nat. Mater.* **13** 439
[34] Cui J, Wu Y M, Muehlbauer J, Hwang Y H, Radermacher R, Fackler S, Wuttig M and Takeuchi I 2012 *Appl. Phys. Lett.* **101** 073904
[35] Schmidt M, Ullrich J, Wieczorek A, Frenzel J, Schütze A, Gunther Eggeler G and Seelecke S 2015 *Shap. Mem. Superelasticity* **1** 132
[36] Chen J Y, Xing L L, Fang G, Lei L P and Liu W 2021 *Acta Mater.* **208** 116741
[37] Qian S X, Ling J Z, Hwang Y H, Radermacher R and Takeuchi I 2015 *Int. J. Refrig* **56** 65
[38] Yuan B, Zhong S J, Qian M F, Zhang X X and Geng L 2021 *J. Alloy. Compd.* **850** 1566612
[39] Zhao Y D, Ning R, Li H, Sun S B, Wang H Z, Gao Y, Zhao D Q, Cao X Z, Gao Z Y and Cai W 2022 *J. Alloy. Compd.* **906** 164280
[40] Li D, Li Z B, Zhang X L, Yang B, Wang D H, Zhao X and Zuo L 2020 *Scr. Mater.* **189** 78
[41] Cui J, Chu Y S, Famodu O O, Furuya Y, Hattrick-Simpers J, James R D, Ludwig A, Thienhaus S, Wuttig M, Zhang Z Y and Takeuchi I 2006 *Nat. Mater.* **5** 286
[42] Wang Y D, Gong B, Wang L, Li S H, Song C, Huang L, Nie Z H, Wang Y D and Cong D Y 2025 *J. Alloy. Compd.* **1040** 183402
[43] Jee K K, Potapov P L, Song S Y and Shin M C 1997 *Scr. Mater.* **36** 207
[44] Wu Z G, Guo J P, Liang Z W, Zhang Y J, Ye X J, Zhang J S, Li Y C, Liu Y N and Yang H 2020 *J. Alloy. Compd.* **829** 154606
[45] Wei Z Y, Liu E K, Chen J H, Li Y, Liu G D, Luo H Z, Xi X K, Zhang H W, Wang W H and Wu G H 2015 *Appl. Phys. Lett.* **107** 022406
[46] Liu C T and Stiegler J O 1984 *Science* **226** 636
[47] Schulson E M, Weihs T P, Baker I, Frost H J and Horton J A 1986 *Acta Mater.* **34** 1395
[48] Liu Y, Liu C T, Heatherly L and George E P 2011 *Scr. Mater.* **64** 303
[49] Liu C T and George E P 1990 *Scr. Metall. Mater.* **24** 1285
[50] Sakamoto H, Kijima Y and Shimizu K I 1982 *Trans. Japn. Inst. Met.* **23** 585
[51] Wilkes K E and Liaw P K 2000 *JOM* **52** 45
[52] Yang Z, Cong D Y, Sun X M, Nie Z H and Wang Y D 2017 *Acta Mater.* **127** 33
[53] Wu X 2006 *Intermetallics* **14** 1114
[54] Tang X H, Feng Y, Wang H B and Wang P 2019 *Appl. Phys. Lett.* **114** 033901
[55] Masdeu F, Pons J, Torrens-Serra J, Chumlyakov Y and Cesari E 2022 *Mat. Sci. Eng. A* **833** 142362
[56] Hernández-Navarro F, Camarillo-Garcia J P, Aguilar-Ortiz C O, Flores-Zúñiga H, Ríos D, González J G and Álvarez-Alonso P 2018 *Appl. Phys. Lett.* **112** 164101
[57] Huang Y J, Hu Q D, Bruno N M, Chen J H, Karaman I, Ross Joseph H and Li J G 2015 *Scr. Mater.* **105** 42
[58] Guan Z, Bai J, Zhang Y, Gu J, Zhang Y, Esling C, Zhao X and Zuo L 2023 *Scr. Mater.* **229** 115353
[59] Li J Z and Li J G 2012 *Mater. Lett.* **68** 40
[60] Zhang G Y, Wang H L, Li Z B, Yang B, Yan H L, Zhao X and Zuo L 2023 *Scr. Mater.* **234** 115584
[61] Huang X M, Zhao Y, Yan H L, Jia N, Tang S, Bai J, Yang B, Li Z B, Zhang Y D, Esling C, Zhao X and Zuo L 2020 *Scr. Mater.* **185** 94
[62] Zhang G Y, Wang Y P, Liu C, Cong D Y, Kuang Y F, Yang J J, Yang B, Zuo L and Li Z B 2025 *Acta Mater.* **301** 121541
[63] Chen Z, Cao Y X, Sun L Y, Sun X M and Cong D Y 2024 *Appl. Phys. Lett.* **125** 223103
[64] Quarini J and Prince A 2004 *Proc. Inst. Mech. Eng. Pt. C J. Mechan. Eng. Sci.* **218** 1175
[65] Wang X B, Pu Z, Yang Q, Huang S K, Wang Z C, Kustov S and Van Humbeeck J 2019 *Scr. Mater.* **163** 57
[66] Aaltio I, Fukuda T and Kakeshita T 2019 *J. Alloy. Compd.* **780** 930
[67] Chen H Y, Zhang X Y, Niu Y R, Cong D Y, Ren Y and Wang Y D 2023 *Jom* **75** 1393
[68] Chluba C, Ge W W, Miranda R L, Strobel J L, Kienle L, Quandt E and Wuttig M 2015 *Science* **348** 1004
[69] Kim Y, Jo M G, Park J W, Park H K and Han H N 2018 *Scr. Mater.* **144** 48
[70] Ahadi A and Sun Q P 2013 *Appl. Phys. Lett.* **103** 021902
[71] Ueland S M and Schuh C A 2013 *Acta Mater.* **61** 5618
[72] Cao Y X, Zhou X L, Cong D Y, Zheng H X, Cao Y H, Nie Z H, Chen Z, Li S H, Xu N, Gao Z Y, Cai W and Wang Y D 2020 *Acta Mater.* **194** 178
[73] Lin H Y, Hua P, Li Y, Li Q, Yu K P, Yan J, Onuki Y, Wang Q H, Su C F, Zhou G A, Sato S, Huang K, Luan J H, Lee Y K, Huang M X, Yang Y, Ren Y and Sun Q P 2026 *Mat. Sci. Eng. A* **949** 149449
[74] Zhou M, Wang W, Su H J, Hu Z J and Li L F 2024 *Chin. Phys. B* **33** 056501
[75] Chen J Y, Zhang K, Kan Q H, Yin H and Sun Q P 2019 *Appl. Phys. Lett.* **115** 093902
[76] Lin H Y, Hua P, Huang K, Li Q and Sun Q P 2023 *Scr. Mater.* **226** 115227
[77] Hua P, Xia M L, Onuki Y and Sun Q P 2021 *Nat. Nanotechnol.* **16** 409
[78] He B B, Hu B, Yen H W, Cheng G J, Wang Z K, Luo H W and Huang M X 2017 *Science* **357** 1029
[79] Liang D S, Wang Q H, Chu K J, Chen J Y, Hua P, Ren F Z and Sun Q P 2022 *Appl. Mater. Today* **26** 101377
[80] Wang Q H, Yin H and Sun Q P 2024 *J. Mater. Res. Technol.* **30** 8906
[81] Chen J Y, Zhao C Q, Zhang S B, Zhang W J, Liu W, Lei L P, Ramamurty U and Fang G 2024 *Mater. Sci. Eng. A* **892** 146073
[82] Chen J Y, Liu B Q, Xing L L, Liu W, Lei L P and Fang G 2022 *Acta Mater.* **226** 117609
[83] Chen J Y, Wang W Q, Zhang Q, Lei L P, Ramamurty U and Fang G 2024 *Scr. Mater.* **245** 116060
[84] Dang P F, Zhou Y M, Pang J B, Ding X D, Sun J, Lookman T and Xue D Z 2023 *Scr. Mater.* **226** 115263
[85] Dang P F, Ye F, Zhou Y M, Ding L, Pang J B, Zhang L, Ding X D, Sun J, Dai S, Lookman T and Xue D Z 2022 *Acta Mater.* **229** 117802
[86] Li S H, Cong D Y, Sun X M, Zhang Y, Chen Z, Nie Z H, Li R G, Li F Q, Ren Y and Wang Y D 2019 *Mater. Res. Lett.* **7** 482
[87] Liu G J, Huang L and Cong D Y 2025 *Mater. Lett.* **394** 138661
[88] Liu H W, Li Z, Zhang Y L, Ni Z T, Xu K and Liu Y S 2020 *Scr. Mater.* **177** 1

[89] Xu X, Nagashima A, Nagasako M, Omori T, Kanomata T and Kainuma R 2017 *Appl. Phys. Lett.* **110** 121906
[90] Liu C, Li D, Li Z B, Yang B, Yan H L, Li J R, Li Z, Zhao X and Zuo L 2021 *Appl. Phys. Lett.* **118** 103904
[91] Niu Y R, Chen H Y, Wang D K, Yang J H, Wang Y D, Li S W, Li T C, Cong D Y, Li S L and Wang Y D 2025 *Mater. Res. Lett.* **13** 1171
[92] Shen A, Zhao D W, Sun W, Liu J and Li C J 2017 *Scr. Mater.* **127** 1
[93] Zhang X Y, Chen H Y, Niu Y R, Li, R G, Yin T, Lang R Q, Song C, Meng L Y, Cong D Y, Li S L and Wang Y D 2022 *Appl. Phys. Lett.* **120** 151903
[94] Zhang X Y, Chen H Y, Li S W, Niu Y R, Yin T, Song C, Lang R Q, Cong D Y, Li S L and Wang Y D 2022 *J. Alloy. Compd.* **918** 165633
[95] Ota T, Ohmori T, Tanaka Y, Morito H, Fujita A, Kainuma R, Fukamichi K and Ishida K 2002 *Appl. Phys. Lett.* **81** 5201
[96] Efstathiou C, Sehitoglu H, Kurath P, Foletti S and Davoli P 2007 *Scr. Mater.* **57** 409
[97] Li Y, Zhao D W and Liu J 2016 *Sci. Rep.* **6** 25500
[98] Pataky G J, Ertekin E and Sehitoglu H 2015 *Acta Mater.* **96** 420
[99] Imran M, Zhang X X, Qian M F and Geng L 2020 *Adv. Eng. Mater.* **22** 1901140
[100] Imran M and Zhang X X 2020 *Phys. Rev. Mater.* **4** 065403
[101] Huang X M, Zhao Y, Yan H L, Jia N, Yang B, Li Z B, Zhang Y D, Esling C, Zhao X, Ren Q Y, Tong X and Zuo L 2023 *Scr. Mater.* **234** 115544
[102] Sutou Y, Omori T, Yamauchi K, Ono N, Kainuma R and Ishida K 2005 *Acta Mater.* **53** 4121
[103] Xu S, Huang H Y, Xie J X, Takekawa, S, Xu, X, Omori T and Kainuma R 2016 *APL Mater.* **4** 106106
[104] Qian S, Geng Y L, Wang Y, Pillsbury T E, Hada Y, Yamaguchi Y, Fujimoto K, Hwang Y H, Radermacher R, Cui J, Yuki Y J, Toyotake K and Takeuchi I 2016 *Philos. T. R. Soc. A* **374** 20150309
[105] Kusama T, Omori T, Saito T, Kise S, Tanaka T, Araki Y and Kainuma R 2017 *Nat. Commun.* **8** 354
[106] Omori T, Kusama T, Kawata S, Ohnuma I, Sutou Y, Araki Y, Ishida K and Kainuma R 2013 *Science* **341** 1500
[107] Lu N H and Chen C H 2021 *Mater. Sci. Eng. A* **800** 140386
[108] Wang Y P, Du H Q, Liu H W, Yang J J, Li Z B, Li J W, Yang B, Yan H L and Zuo L 2024 *Scr. Mater.* **252** 116227
[109] Guo Y Z, Wang Y P, Liu H W, Du H Q, Liu C, Cong D Y, Yang J J, Li J W and Li Z B 2025 *J. Alloy. Compd.* **1041** 183727
[110] Fan Z M, Li X, Zhang P N, Zhai Q J, Wang G, Li Q and Liu J 2025 *Scr. Mater.* **261** 116603
[111] Li X, Fan Z M, Zhai Q J, Wang G, Lu X, Qian H Y, Cai R, Jiang D Q and Liu J 2025 *Addit. Manuf. Lett.* **13** 100281
[112] Li Q, Deng Z Z, Ahadi A, Chu K J, Yan J, Huang K, Hu S X, Ren Y, He B B and Sun Q P 2025 *Nat. Commun.* **16** 4511